Modeling Ca^{2+} Feedback on a Single Inositol 1,4,5-Trisphosphate Receptor and Its Modulation by Ca^{2+} Buffers

Jianwei Shuai,*† John E. Pearson,‡ and Ian Parker†§

*Department of Physics, Xiamen University, Xiamen, China; †Department of Neurobiology & Behavior, University of California, Irvine, California; ‡Applied Theoretical and Computational Physics, Los Alamos National Laboratory, Los Alamos, New Mexico; and §Department of Physiology & Biophysics, University of California, Irvine, California

ABSTRACT The inositol 1,4,5-trisphosphate receptor/channel (IP_3R) is a major regulator of intracellular Ca^{2+} signaling, and liberates Ca^{2+} ions from the endoplasmic reticulum in response to binding at cytosolic sites for both IP_3 and Ca^{2+}. Although the steady-state gating properties of the IP_3R have been extensively studied and modeled under conditions of fixed [IP_3] and [Ca^{2+}], little is known about how Ca^{2+} flux through a channel may modulate the gating of that same channel by feedback onto activating and inhibitory Ca^{2+} binding sites. We thus simulated the dynamics of Ca^{2+} self-feedback on monomeric and tetrameric IP_3R models. A major conclusion is that self-activation depends crucially on stationary cytosolic Ca^{2+} buffers that slow the collapse of the local [Ca^{2+}] microdomain after closure. This promotes burst-like reopenings by the rebinding of Ca^{2+} to the activating site; whereas inhibitory actions are substantially independent of stationary buffers but are strongly dependent on the location of the inhibitory Ca^{2+} binding site on the IP_3R in relation to the channel pore.

INTRODUCTION

The inositol 1,4,5-trisphosphate receptor (IP_3R) is a Ca^{2+} release channel that liberates Ca^{2+} ions from the endoplasmic reticulum (ER) into the cytoplasm upon the binding of both inositol 1,4,5-trisphosphate (IP_3) and Ca^{2+} itself (1–4). The biphasic positive and negative feedback of Ca^{2+} ions on IP_3R gating underlies the complexity of Ca^{2+} signals observed in intact cells, including Ca^{2+} ''blips'' that may represent openings of individual channels (5–7), local transients (Ca^{2+} ''puffs'') restricted to clusters containing several IP_3Rs (5,8,9), as well as global Ca^{2+} waves that propagate throughout the cell (10,11). An understanding of the Ca^{2+} feedback actions at the single channel level is crucial, since they underlie the complex hierarchy of local cytosolic calcium signals and global oscillations seen in cell types as diverse as smooth muscle and neurons (3,5,11). Correspondingly, however, this complexity makes it difficult to elucidate the functional properties of single IP_3R under conditions where Ca^{2+} feedback is active (4,12). Instead, most of our detailed knowledge of IP_3R gating derives from patch-clamp and bilayer recording of single IP_3R channels under conditions where ions other than Ca^{2+} serve as the charge carrier, and where [Ca^{2+}] on the cytosolic face is ''clamped'' at fixed levels by buffers (4,13,14). Another difficulty to study blip events is that the opening of one IP_3R channel usually triggers openings of multiple adjacent channels in the cluster on ER membrane.

In addition to the IP_3R dynamics, endogenous Ca^{2+} binding buffers also play a key role in determining the magnitude, kinetics, and spatial distribution of cytosolic Ca^{2+} signals (15,16). Different cell types selectively express mobile Ca^{2+} binding proteins with differing properties (17), suggesting that cells likely utilize buffers to shape Ca^{2+} signals for their specific function (15,16).

Models of IP_3R play an important role not only for understanding single channel kinetics, but also as building blocks for constructing larger-scale models of cellular Ca^{2+} signaling. Different IP_3R models have been suggested (18–23) and the calcium release dynamics have also been discussed accordingly, which are mainly at the level of local Ca^{2+} puffs (24–27) or at the level of global Ca^{2+} waves (28–32). However, due to the paucity of experimental data on blips, there are few modeling studies of single IP_3R function within a cellular environment (33,34). Swillens et al. (33) proposed a monomeric IP_3R model to account for the electrophysiological data obtained with an IP_3R channel incorporated in a planar bilayer, and then explored the Ca^{2+} blip dynamics that result by placing the channel model in a realistic physiological environment. The simulated blip exhibited bursts of activity, arising from repetitive channel openings caused by the Ca^{2+} rebinding to the activating site due to the high Ca^{2+} concentration at the channel mouth just after closure. Furthermore, they noted that the amplitudes and rising times of the simulated blips are highly sensitive to buffering by the Ca^{2+} indicator dye.

The effects of endogenous Ca^{2+} buffers have also been investigated analytically and numerically (35–38). It was suggested that the rapid buffer could be approached by a rapid buffering approximation near a point source on timescales that are comparable to the equilibration times for Ca^{2+} buffers (36,37). With a stochastic IP_3R model, the effects of slow buffer on the intracellular Ca^{2+} waves have been investigated, indicating that the high concentration of slow buffer can lead to an oscillatory behavior by repetitive wave nucleation for high Ca^{2+} content of the ER (38).

Submitted May 9, 2008, and accepted for publication July 16, 2008.

Address reprint requests to Dr. Jianwei Shuai, Dept. of Physics, Xiamen University, Xiamen, Fujian 361005, China. Tel.: 86-592-218-2575; Fax: 86-592-218-9426; E-mail: jianweishuai@xmu.edu.cn.

Editor: Arthur Sherman.

0006-3495/08/10/3738/15 $2.00

doi: 10.1529/biophysj.108.137182

Here, we explore in detail the dynamics of blips and their modulation by immobile cytosolic Ca^{2+} buffers using an IP_3R model proposed recently (39). This study represents an intermediate step toward our long-term goal to bridge the gap between single-channel studies and whole-cell Ca^{2+} imaging by using theoretical simulations to develop a unified model of IP_3/Ca^{2+} signaling. We focus on the *Xenopus* oocyte as a model cell system, owing to the wealth of published experimental data on both single-IP_3R properties (14) and cellular imaging studies (6,9). As a first step, we recently described a stochastic IP_3R model (39) that satisfactorily replicated the steady-state gating kinetics of the *Xenopus* IP_3R under conditions of fixed cytosolic $[Ca^{2+}]$. We now extend this model to explore the effects of Ca^{2+} feedback, whereby Ca^{2+} flux through a single channel modulates the gating of that same channel via binding to activating and inhibitory sites on the IP_3R molecule.

Our full IP_3R model (39) is composed of four independent, identical subunits, each of which bears one IP_3 binding site, one activating Ca^{2+} binding site, and one inhibitory Ca^{2+} binding site (Fig. 1 *A*). A subunit may enter an ''active'' conformation when the IP_3 and activating (but not inhibitory) Ca^{2+} binding sites are occupied, and the channel opens when either three or four subunits are active. Two features of this model are of particular importance with regard to the ability of Ca^{2+} ions passing through the channel to bind to receptor sites on the cytosolic face and thereby modulate channel gating. First, transition to the active state of a subunit incorporates a conformational change such that the active state is ''locked'' to ligand binding: that is to say, Ca^{2+} cannot bind to or dissociate from either the activating or inhibitory sites of an active subunit. Ca^{2+} flux through an IP_3R channel cannot, therefore, directly act on active subunits while the channel is open. Secondly, the assumption that only three subunits need to be active for the channel to open leads to an additional and more subtle modulation, because the high local $[Ca^{2+}]$ around the pore of an open channel results in a high probability of binding to the low-affinity inhibitory site of the remaining inactive subunit.

Openings of single IP_3R channels are believed to underlie ''fundamental'' IP_3-mediated signals, such as Ca^{2+} blips (5,6) and trigger events (40,41) that serve a crucial role in initiating larger scale local and global responses through Ca^{2+}-induced Ca^{2+} release from neighboring channels. Our results provide important insights into the generation of these fundamental events, particularly regarding the effect of immobile cytosolic Ca^{2+} buffers in modulating feedback onto the IP_3R by enhancing the activating Ca^{2+} rebinding actions, whereas the inhibitory binding dynamics are substantially independent of stationary buffers but are strongly dependent on the location of the inhibitory Ca^{2+} binding site on the IP_3R in relation to the channel pore. The model, moreover, serves as a necessary stepping stone to construct stochastic models of the interactions among IP_3Rs within a cluster.

METHODS

The IP_3R subunit model

Our IP_3R model (39) is derived from the original DeYoung-Keizer formulation (18), and is composed of four independent, identical subunits, each bearing one IP_3 binding site, one activating Ca^{2+} binding site, and one inhibitory Ca^{2+} binding site (Fig. 1 *A*). A conformational step is introduced before a subunit becomes active. The subunit state is denoted (*i j k*), where *i* represents the IP_3 binding site, *j* the activating Ca^{2+} binding site, and *k* the inhibitory Ca^{2+} binding site. The number 1 represents an occupied site and 0 a nonoccupied site. Bold arrows in Fig. 1 *A* indicate the binding of ligands to different sites, and the shaded regions indicate conformations referred to as ''active'', ''inactive'' (without Ca^{2+} bound to the inhibitory site), and ''inhibited'' (with Ca^{2+} bound to the inhibitory site).

In our simulations, we begin by considering a simplified ''toy'' model wherein channel opening requires only a single active subunit so as to gain a better intuitive understanding of the actions of Ca^{2+} feedback, and then progress to a more realistic tetrameric model in which channel opening requires 3 or 4 active subunits.

Stochastic simulations and Ca^{2+} current of the IP_3R channel

We simulated the stochastic dynamics of the nine-state IP_3R subunit model by a Markov process, updating the state of the system at small time steps

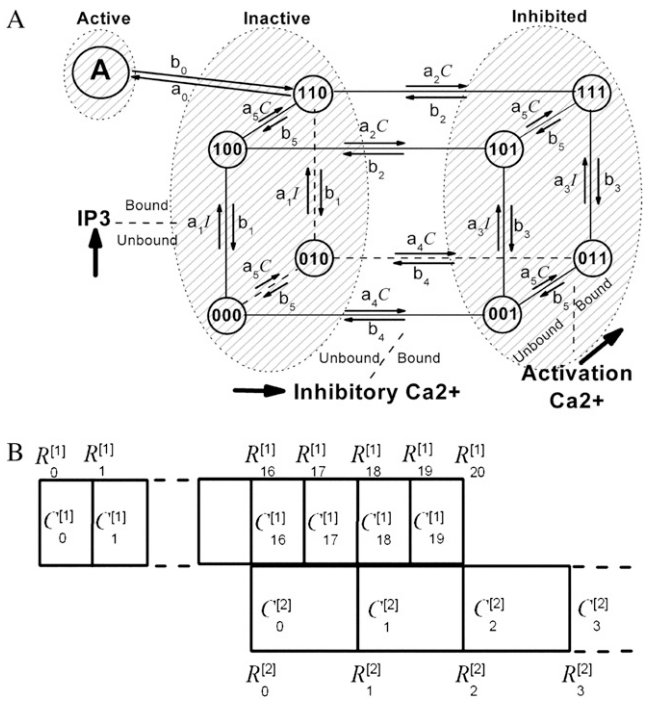

FIGURE 1 IP_3R subunit model and the multiple-grid-size method. (*A*) Schematic diagram of the IP_3R channel subunit model. The subunit has an IP_3 binding site, an activating Ca^{2+} binding site, and an inhibitory Ca^{2+} binding site. Bold arrows indicate the binding of ligands to different sites, and the shaded regions indicate conformations referred to as active, inactive (without Ca^{2+} bound to the inhibitory site), and inhibited (with Ca^{2+} bound to the inhibitory site). (*B*) In the model, we use a multiple-grid-size method to discretize the cytosolic space. An overlap region is used to connect the concentration in different regions. So concentration $C_0^{[2]}$ at $R_0^{[2]}$ is an average of the concentration $C_{16}^{[1]}$ at $R_{16}^{[1]}$ and $C_{17}^{[1]}$ at $R_{17}^{[1]}$.

$dt = 1\ \mu$s. For example, a channel subunit in the (110) state at time t could transition to states (010), (100), (111), or to the active state at the next time step $t+dt$ with respective transition probabilities of $b_1 dt,\ b_5 dt, a_2[Ca^{2+}] \times dt$, or $a_0 dt$; otherwise it would remain in the same state. Random numbers homogeneously distributed in [0,1] were generated at each time step and compared with these transition probabilities to determine the state of the channel subunit at the next time step.

A constant Ca^{2+} current I_{Ch} flows through an open channel from the ER into cytosolic space. The Ca^{2+} flux is expressed as

$$J_{Ch} = \frac{I_{Ch}}{2 \times F \times \delta V}, \tag{1}$$

where $F = 9.65 \times 10^{-11} C/fmol$ and $\delta V = \pi \times (\Delta r)^3/6$ is the spherical volume around the channel pore with radius $\Delta r/2$.

In the model, we assume a constant Ca^{2+} current (flux) through an open IP_3R channel, i.e., $I_{Ch} = 0.2$ pA. The single-channel IP_3R Ca^{2+} current that we assume here is within the range of 0.2–0.5 pA estimated in our previously published article (42), in which a detailed modeling study was presented for the fluorescence signals that would result from Ca^{2+} flux through a single IP_3R, taking into account factors including diffusion, binding to indicator dye and cytosolic buffers, and the point-spread function of the confocal microscope, to provide good agreement with experimental imaging data.

An alternative approach is to assume a Ca^{2+} flux that is proportional to the difference of free Ca^{2+} concentrations between the ER pool and the cytosolic space around the channel pore. Local depletion of Ca^{2+} in the ER pool may then reduce the Ca^{2+} flux throughout an open channel, as proposed for sparks in cardiac and skeletal muscle. However, such luminal depletion appears to be minimal for isolated puffs released from a few open channels in *Xenopus* oocytes, as observations of sequential puffs at intervals of a few hundred ms show little diminution in amplitude of the second puffs (43). Thus, a simple assumption is to consider a fixed ER Ca^{2+} concentration (e.g., 500 μM). In that case, our simulations indicate the Ca^{2+} current approaches an almost constant value within 1 ms after channel opening, which can be well approximated by a constant Ca^{2+} flux as used in our model.

Cytosolic Ca^{2+} diffusion

In this article, our goal was to study the dynamics of the single IP_3R channel within a cytosolic-like environment. In that regard, we made several simplifying assumptions; neglecting Ca^{2+} pump dynamics (which are slow on the timescales considered here) and endogenous mobile buffers. Specifically, the model includes the following species in the cytosolic space: free Ca^{2+} ions ($[Ca^{2+}]$), stationary buffer in free and Ca^{2+}-bound ([SCa]) forms, and mobile buffer in free and Ca^{2+}-bound ([MCa]) forms. In comparison to the large cytosolic volume, we treat the ER pool as an ideal point source occupying no volume.

A further simplification is that we calculate the transition probabilities of binding kinetics as functions of the calcium concentration at one grid point. Because of the exceedingly small volume with $\Delta r = 5$ nm associated with each grid point, the mean numbers of Ca^{2+} ions within that volume will typically be <1, introducing large stochastic fluctuations. However, it is computationally impracticable to undertake a particle simulation considering every individual ion. Instead, we justify our method of deterministic reaction-diffusion treatment for Ca^{2+} concentration by considering that characteristic binding times to sites on IP_3R and buffers are of the order of milliseconds or even hundreds of milliseconds, whereas diffusional exchange of free Ca^{2+} ions within a grid volume with $\Delta r = 5$ nm will occur within only about $(\Delta r)^2/D = 0.125\ \mu$s for diffusion coefficient $D = 200\ \mu m^2/s$, thereby averaging out fluctuations on the timescales of interest (34).

The diffusion equation for free Ca^{2+} ions ($[Ca^{2+}]$) with diffusion coefficient D is described as follows:

$$\begin{aligned}\frac{\partial[Ca^{2+}]}{\partial t} &= D\nabla^2[Ca^{2+}] + \delta_0 \times J_{Ch} \\ &\quad + \beta_S \times [SCa] - \alpha_S \times [Ca^{2+}] \times (S_T - [SCa]) \\ &\quad + \beta_M \times [MCa] - \alpha_M \times [Ca^{2+}] \times (M_T - [MCa]),\end{aligned} \tag{2}$$

in which the function $\delta_0 = 1$ at the origin point represents the channel location; otherwise, $\delta_0 = 0$. The total concentrations of Ca^{2+} stationary buffer and mobile buffer are S_T and M_T, respectively, and α is the Ca^{2+} bound rate and β the Ca^{2+} unbound rate for buffers. For Ca^{2+}-bound stationary buffer ([SCa]) with diffusion coefficient D_{MCa},

$$\frac{\partial[SCa]}{\partial t} = \alpha_S \times C \times (S_T - [SCa]) - \beta_S \times [SCa]. \tag{3}$$

For Ca^{2+}-bound mobile buffer ([MCa]) with diffusion coefficient D_{MCa},

$$\begin{aligned}\frac{\partial[MCa]}{\partial t} &= D_{MCa}\nabla^2[MCa] + \alpha_F \times [Ca^{2+}] \times (M_T - [MCa]) \\ &\quad - \beta_F \times [MCa].\end{aligned} \tag{4}$$

We simulate the propagation of Ca^{2+} throughout a homogeneous three-dimensional cytosolic space. Following from the spherical symmetry around the channel pore, Ca^{2+} diffusion can be described in spherical coordinates with the Laplacian operator

$$\nabla^2[Ca^{2+}](r,t) = \frac{2}{r} \times \frac{\partial}{\partial r}[Ca^{2+}](r,t) + \frac{\partial^2}{\partial r^2}[Ca^{2+}](r,t). \tag{5}$$

Thus, we calculate the time-dependent distribution of Ca^{2+} concentration along the radial direction.

The numerical method for Ca^{2+} diffusion

The finite difference method proposed by Smith et al. (37) was used to solve the partial differential equations. Considering a time increment Δt and spatial grid distance Δr, an explicit numerical scheme for the calcium diffusion that is second-order accurate in space and first-order accurate in time is then given by

$$\begin{aligned}C_0(n+1) &= C_0(n) + 6 \times D \times \frac{\Delta t}{\Delta r^2}(C_0(n) - C_0(n)) \\ &\quad + \Delta t \times J_{Ch}^n(n) + \Delta t \times \Delta S_0(n) + \Delta t \times \Delta M_0(n) \\ C_i(n+1) &= C_i(n) + D \times \frac{\Delta t}{\Delta r^2}\left(\left(\frac{R_{i+1/2}}{R_i}\right)^2 (C_{i+1}(n) - C_i(n))\right. \\ &\quad \left. - \left(\frac{R_{i-1/2}}{R_i}\right)^2 (C_i(n) - C_{i-1}(n))\right) + \Delta t \times \Delta S_i(n) \\ &\quad + \Delta t \times \Delta M_i(n) \quad i = 1,2,\cdots,N,\end{aligned} \tag{6}$$

where $C_i(n)$ represents the free calcium concentration at location $R_i = i \times \Delta r$ and time $t_n = n \times \Delta t$; $\Delta S_i(n)$, and $\Delta M_i(n)$ denote the contribution of the reaction terms with stationary buffer and mobile buffer at location $i\Delta r$ and time $n\Delta t$, respectively:

$$\begin{aligned}\Delta S_i^n &= \beta_S \times [SCa]_i^n - \alpha_S \times C_i^n \times (S_T - [SCa]_i^n) \\ \Delta M_i^n &= \beta_M \times [MCa]_i^n - \alpha_M \times C_i^n \times (M_T - [MCa]_i^n),\end{aligned} \tag{7}$$

where $[SCa]_i(n)$ and $[MCa]_i(n)$ represent the concentrations of Ca^{2+}-bound stationary buffer and mobile buffer at location $i\Delta r$ and time $n\Delta t$, respectively. For stationary buffer $[SCa]_i(n)$, we have

$$[SCa]_i(n+1) = [SCa]_i(n) - \Delta t \times \Delta S_i(n), i = 0, 1, 2, \cdots, N. \quad (8)$$

For mobile buffer $M_i(n)$ at location $i\Delta r$ and time $n\Delta t$, the difference equations are similar as given in Eq. 6.

The total radius of the simulated cytosolic space is $R = 3.2$ μm. To enhance the computation speed, we applied a multiple-grid-size method to discretize the cytosolic space as follows: for the first regime at $r \le 0.1$ μm, $\Delta r_1 = 5$ nm with 20 grids that are marked as $R_i^{[1]}$ with the superscript ''[1]'' corresponding to the smallest grid region; for the second regime at $0.08 \le r \le 0.28$ μm, $\Delta r_2 = 10$ nm with 20 grids marked as $R_i^{[2]}$; for $0.24 \le r \le 0.64$ μm, $\Delta r_3 = 20$ nm with 20 grids; for $0.56 \le r \le 1.36$ μm, $\Delta r_4 = 40$ nm with 20 grids; and for $1.2 \le r \le 3.2$ μm, $\Delta r_5 = 80$ nm with 25 grids. Thus there is an overlap between each two connected regions. Overlap regions are used to ensure that the calcium concentrations at the same position, but with different grid sizes, are connected correctly. For example, as shown in Fig. 1 *B*, the calcium concentration $C_0^{[2]}$ at $R_0^{[2]}$ is an average of the concentration $C_{16}^{[1]}$ at $R_{16}^{[1]}$ and $C_{17}^{[1]}$ at $R_{17}^{[1]}$ with different volume weight. Thus we have

$$C_0^{[2]} = \frac{\left((R_{17}^{[1]})^3 - (R_{16}^{[1]})^3\right) \times C_{16}^{[1]} + \left((R_{18}^{[1]})^3 - (R_{17}^{[1]})^3\right) \times C_{17}^{[1]}}{(R_1^{[2]})^3 - (R_0^{[2]})^3}. \quad (9)$$

Here the superscript in brackets corresponds to the different grid refinement Δr_j considered and the subscript corresponds to the ordering i within the grid set. We can write out the similar equation for $C_1^{[2]}$, and then we have

$$C_{19}^{[1]} = \frac{\left((R_2^{[2]})^3 - (R_1^{[2]})^3\right) \times C_1^2 - \left((R_{19}^{[1]})^3 - (R_{18}^{[1]})^3\right) C_{18}^{[1]}}{(R_{20}^{[1]})^3 - (R_{19}^{[1]})^3}. \quad (10)$$

These two equations are used for the determination of boundary condition of free Ca^{2+} concentration at different grid-size regions. Similar equations can be given for stationary buffer and mobile buffer.

The resting concentration of free Ca^{2+} ions $[Ca^{2+}]_{Rest} = 0.05$ μM. Then the resting concentrations of stationary buffer and mobile buffer are $S_T/(1+\beta_S/(\alpha_S \times [Ca^{2+}]_{Rest}))$ and $M_T/(1+\beta_M/(\alpha_M \times [Ca^{2+}]_{Rest}))$, respectively. At the boundaries of the system, the concentrations of all signal species are held constant at their resting states. Because the smallest grid size $\Delta r = 5$ nm, the calcium concentration is updated with time step $\Delta t = 0.02$ μs.

Parameter values

The parameter values used in the model are given in the Table 1. For the IP_3R channel kinetics, dissociation constants $K_i = b_i/a_i$ with a_i on-binding rate and b_i off-binding rate. Due to the thermodynamic constraint, we have $K_1K_2 = K_3K_4$. The binding and unbinding rates of the IP_3R channel are taken mainly from our earlier study (39), excepting that the rate constant a_5 for activating Ca^{2+} binding was reduced to 30 $\mu M^{-1}s^{-1}$ to match recent experimental measurements of long first-opening latencies of IP_3R channels in Sf9 cell nuclei at $[IP_3] = 10$ μM after step increases in $[Ca^{2+}]$ from 0 to 2.5 μM (44). It was shown that the channel activation by a jump from low (<10 nM) to optimal (2 μM) $[Ca^{2+}]$ had a mean latency of 40 ms, and the channel deactivation when Ca^{2+} was returned to <10 nM from 2 μM had a mean latency of 160 ms (44). For the current model with the modified a_5, the mean latency for Ca^{2+} activation binding is 20 ms and the mean latency for Ca^{2+} deactivation unbinding is 170 ms. As a comparison, the previous IP_3R model gave the mean latencies of 80 ms and 280 ms for activation and deactivation, respectively (39).

TABLE 1 Parameter values used in the model

	Parameter	Value (unit)
System size	R	3.2 μm
Free Ca^{2+}	$[Ca^{2+}]_{Rest}$	0.05 μM
	D	200 $\mu m^2/s$
Stationary Ca^{2+} buffer	S_T	0 ~ 10,000 μM
	α_S	400 $\mu M^{-1}s^{-1}$
	β_S	800 s^{-1}
Mobile Ca^{2+} buffer	S_T	0 ~ 1000 μM
	D_{MCa}	1 ~ 200 $\mu m^2/s$
	α_S	150 $\mu M^{-1}s^{-1}$
	β_S	300 s^{-1}
IP_3 concentration	$[IP_3]$	0.001 ~ 50 μM
Channel current	I_{Ch}	0.2 pA
Conformation change rate	a_0	540 s^{-1}
	b_0	80 s^{-1}
Channel IP_3 binding site	K_1	0.0036 μM
	a_1	60 $\mu M^{-1}s^{-1}$
	K_3	0.8 μM
	a_3	5 $\mu M^{-1}s^{-1}$
Channel activating Ca^{2+} binding site	K_5	0.8 μM
	a_5	30 $\mu M^{-1}s^{-1}$
Channel inhibitory Ca^{2+} binding site	K_2	16 μM
	a_2	0.04 $\mu M^{-1}s^{-1}$
	K_4	0.072 μM
	a_4	0.5 $\mu M^{-1}s^{-1}$

RESULTS

The Ca^{2+} microdomain around an IP_3R channel pore

The ability of Ca^{2+} ions that have passed through an IP_3R channel to bind to modulatory sites on the cytosolic domain of that channel depends crucially on the spatial and temporal dynamics of the local cytosolic microdomain of Ca^{2+} around the channel pore. We thus began by making deterministic simulations of this local Ca^{2+} distribution during and after channel openings, and explored the effects of stationary Ca^{2+} buffer on the microdomain.

Fig. 2 *A* plots the radial $[Ca^{2+}]$ distribution around the pore immediately before the end of a 20 ms channel opening, and at different times after the channel closes. Fig. 2 *B* shows the corresponding time courses of $[Ca^{2+}]$ at different distances from the pore. In this example, no buffers are present, and Ca^{2+} ions diffuse freely in aqueous medium with a diffusion coefficient of 200 $\mu m^2/s$. The main qualitative results are that an extremely steep Ca^{2+} gradient is established very quickly after the channel opens, and that this subsequently collapses rapidly after channel closing to leave a residual microdomain extending over a few μm that persists for several ms (Fig. 2 *A*). For example, the local $[Ca^{2+}]$ in the grid element at the channel pore rises as high as 400 μM while the channel is open, but at a distance of 15 nm (corresponding to the dimensions of the IP_3R molecule (2)), the concentration is only ~27 μM. Once the channel closes, $[Ca^{2+}]$ at the pore drops

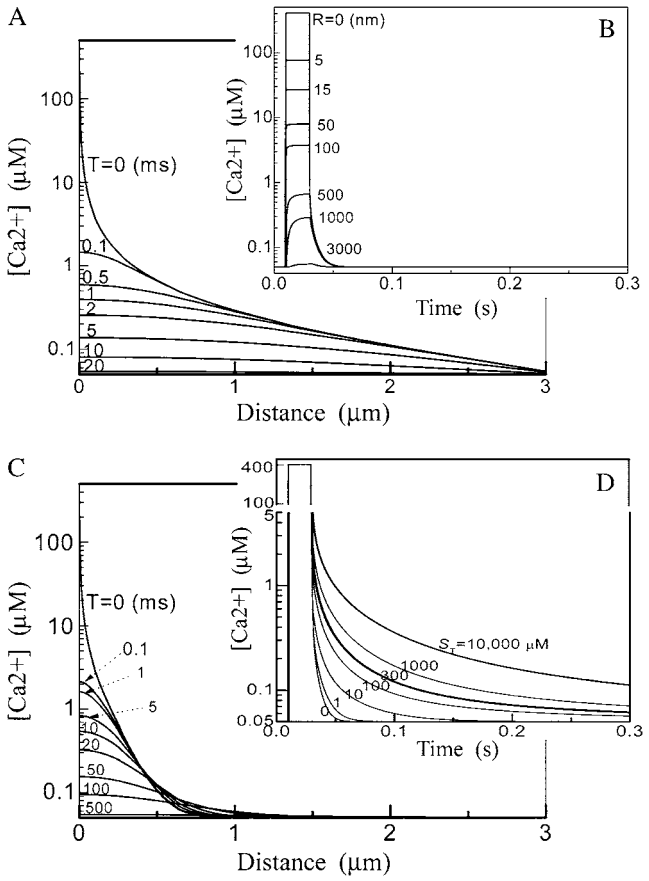

FIGURE 2 $[Ca^{2+}]$ distribution around the channel mouth. (*A* and *B*) Spatial and temporal distributions of cytosolic $[Ca^{2+}]$ around the pore of an IP_3R channel in the absence of any Ca^{2+} buffer. The channel is assumed to open for 20 ms, carrying a Ca^{2+} current of 0.2 pA. (*A*) Spatial $[Ca^{2+}]$ distribution as a function of distance from the channel pore at the instant before channel closes ($T = 0$) and at different times (indicated in ms) after closing. (*B*) Temporal changes in $[Ca^{2+}]$ at the channel pore ($R = 0$ nm) and at different distances (indicated in nm) from the pore. (*C* and *D*) Corresponding simulations with stationary Ca^{2+} buffer in the cytosolic space. (*C*) Spatial $[Ca^{2+}]$ distributions at $T = 0$ and at different times after the channel closed, for a stationary buffer concentration $S_T = 300$ μM. (*D*) Temporal traces of $[Ca^{2+}]$ at channel pore for different stationary buffer concentrations as indicated in μM.

precipitously to 0.5 μM within 0.5 ms, and the radial gradient collapses such that concentrations in the residual microdomain are almost the same at the pore and the channel edge.

This residual microdomain plays a key role in modulating IP_3R function in our model, since Ca^{2+} cannot bind to regulatory sites of active subunits in an open channel. Immobile cytosolic Ca^{2+} buffer exerts two prominent effects on the spatiotemporal properties of the microdomain (Fig. 2, *C* and *D*). There are two prominent effects. i), The spread of free $[Ca^{2+}]$ around an open or recently closed channel narrows from several μm to <1 μm because of the reduction in effective diffusion coefficient for Ca^{2+} (Fig. 2 *C*). ii), The decay of local free $[Ca^{2+}]$ after channel closure becomes greatly slowed because the buffer acts as a reservoir, continuing to release free Ca^{2+} ions that had become bound while the channel was open (Fig. 2 *D*). Fig. 2 *D* further shows how the free $[Ca^{2+}]$ decay rate at the channel pore slows as a function of increasing concentration of immobile buffer. For example, whereas free $[Ca^{2+}]$ at the pore drops to 100 nM within 8 ms after the channel closes in the absence of buffering, the same fall in concentration requires >140 ms in the presence of 1 mM immobile buffer.

The simplified monomeric IP_3R model

To gain an intuitive understanding of how IP_3R gating is modulated by Ca^{2+} feedback from Ca^{2+} passing through the channel, we first consider a simplified monomeric toy model, wherein gating is controlled by only a single subunit; i.e., a channel that has only a single functional subunit and opens when that subunit is in the active state.

Bursting behavior of the monomeric IP_3R model

For purposes of comparison, we first discuss the channel open/close dynamics when cytosolic $[Ca^{2+}]$ is fixed at the resting concentration of 0.05 μM (Fig. 3 *A*), and then consider how these dynamics are modified by feedback of Ca^{2+} flowing through the channel in the absence (Fig. 3 *B*) or presence of stationary Ca^{2+} buffer (Fig. 3 *C*). In these examples, no mobile buffers are present. Fig. 3 *A* illustrates typical channel dynamics for $[IP_3] = 10$ μM when Ca^{2+} is not the charge carrier and cytosolic free $[Ca^{2+}]$ is fixed at 0.05 μM, so as to simulate typical conditions in patch-clamp experiments (14). The channel gating shows a bursting characteristic (*top panel* in Fig. 3 *A*), dominated by the binding and unbinding Ca^{2+} to the activating site (*bottom panel* in Fig. 3 *A*), since the affinity for inhibitory Ca^{2+} binding is low ($K_2 = 16$ μM) in comparison to the basal $[Ca^{2+}]$ and the subunit is primarily in IP_3-bound states. The dynamics within a burst result largely from fast, ligand-independent transitions between the active state and (110) states, with longer interburst intervals largely reflecting dwell times in the (100) state with durations $= 1/a_5[Ca^{2+}] = 0.67$ s for $[Ca^{2+}] = 50$ nM. Fig. 4 *A* (*solid curve*) shows the dependence of P_O on $[IP_3]$, derived by the transition matrix theory (see Appendix A).

Ca^{2+} feedback effect on the monomeric IP_3R in the absence of any buffers

Next, we consider how the dynamics of the simplified, monomeric IP_3R model are modified when Ca^{2+} ions flow through the channel, creating a cytosolic Ca^{2+} microdomain in which Ca^{2+} ions may bind to the activating and inhibitory sites in the absence of any Ca^{2+} buffers. We numerically solve Ca^{2+} diffusion by a finite difference method and initially consider only free aqueous diffusion, unmodified by the presence of any Ca^{2+} buffers. An example of the resulting channel dynamics is given in Fig. 3 *B* for $[IP_3] = 10$ μM,

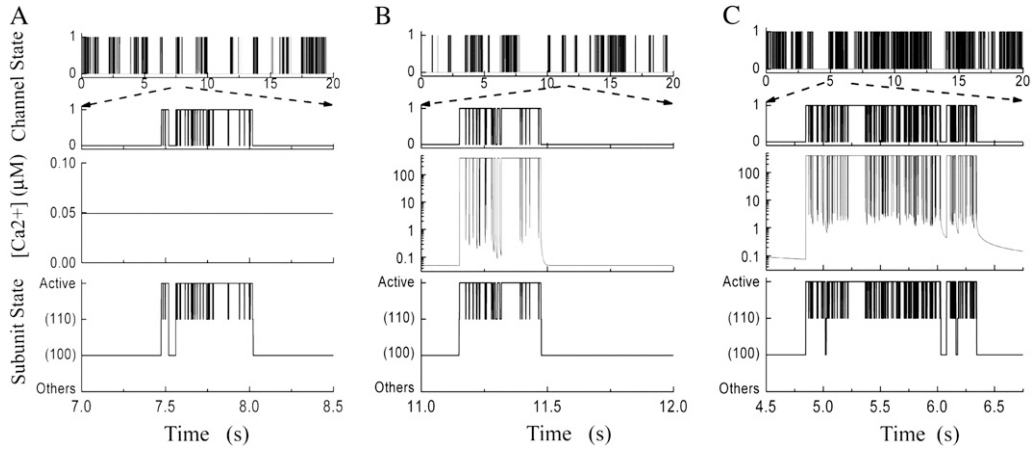

FIGURE 3 (*A*) Representative dynamics of the monomeric model with $[Ca^{2+}]$ clamped at 0.05 μM and $[IP_3] = 10$ μM. The upper panel illustrates bursting behavior of channel states (0 = closed, 1 = open) on a slow timescale, and the second panel shows channel gating during a single burst on an expanded timescale. The third panel shows local $[Ca^{2+}]$ at the channel pore, and the lower panel shows transitions between different subunit states during the burst. (*B*) Corresponding examples of channel, $[Ca^{2+}]$ and subunit dynamics for the case where Ca^{2+} ions flow through the channel. No Ca^{2+} buffers are present. $[IP_3] = 10$ μM. (*C*) Monomeric IP_3R model dynamics with Ca^{2+} flux in the presence of stationary buffer $S_T = 300$ μM in the cytosolic compartment. $[IP_3] = 10$ μM.

which can be directly compared to the corresponding dynamics with fixed cytosolic $[Ca^{2+}]$ (Fig. 3 *A*). A surprising result is that the IP_3R displays qualitatively similar burst-type dynamics (*top panels* in Fig. 3, *A* and *B*) irrespective of whether local cytosolic $[Ca^{2+}]$ is clamped (*third panel* in Fig. 3 *A*) or changes with Ca^{2+} flux through the channel (*third panel* in Fig. 3 *B*). As shown in Fig. 4 *A*, the close similarity of simulation results obtained with Ca^{2+} as the flux carrier (*square symbols*) with clamped Ca^{2+} (*solid line*) further shows that Ca^{2+} feedback has little quantitative effect on the dependency of P_o as a function of $[IP_3]$, even though the activating and inhibitory Ca^{2+} binding sites are located at the channel pore where they experience maximal changes in $[Ca^{2+}]$. Thus, in the absence of Ca^{2+} buffers, Ca^{2+} feedback has little influence on P_o.

The explanation for this arises principally from our assumption that subunit activation requires a preceding conformational step, so that when the channel is open (i.e., the single subunit in the monomeric model is in the active conformation), Ca^{2+} cannot bind to the inhibitory site or dissociate from activating site (Fig. 1 *A*). Thus, Ca^{2+} ions fluxing through the pore cannot modify the IP_3R dynamics while the channel is open, and any feedback is limited to whatever residual Ca^{2+} remains in the microdomain after the channel has closed and the subunit has exited the active state. Immediately after the channel closes, $[Ca^{2+}]$ at the pore mouth falls precipitously; e.g., from 400 μM to 1 μM within 0.1 ms and then to 0.1 μM after ~5 ms. To elucidate why this ''tail'' of $[Ca^{2+}]$ does not change the channel dynamics significantly, we then calculated (see Appendix B for details) the cumulative probabilities of Ca^{2+} binding to the activating site and inhibitory sites as functions of time after channel closure (*solid curves*, Fig. 4, *B* and *C*, respectively), and compared these with corresponding binding probabilities for the case of a fixed cytosolic $[Ca^{2+}]$ of 0.05 μM (*dashed curves*, Fig. 4, *B* and *C*). Although the activating and inhibitory Ca^{2+} binding probabilities in the case of Ca^{2+} ion as the flux carrier are greater than those in the case of clamped Ca^{2+}, the absolute differences between them are slight (increased probability of ~0.025 for binding to the activating site and 0.0008 for inhibitory binding), so that the likelihood of Ca^{2+}-dependent activation or inhibition is minimal during the brief time before the local $[Ca^{2+}]$ collapses down to the basal resting level.

Modulation of Ca^{2+} feedback by stationary buffer

Given that the persistence of the Ca^{2+} microdomain after channel closure is critical for determining whether Ca^{2+} flux can significantly modulate the channel gating, we then considered the effects of immobile Ca^{2+} buffer in modifying the dynamics of the Ca^{2+} microdomain. Fig. 3 *C* shows an example of channel dynamics with the monomeric model under identical conditions to those considered above, except that immobile cytosolic buffer is introduced at a concentration $S_T = 300$ μM. This results in a dramatic increase in open probability and a prolongation of burst durations. For example, for $[IP_3] > 0.05$ μM, P_O is ~3 times greater in the presence of 300 μM stationary buffer than without buffer (Fig. 4 *A*, *dotted curve*).

The reason why stationary buffer increases P_O is given as follows. Once the channel closes when the subunit transitions from the active state to state (110), free $[Ca^{2+}]$ collapses extremely rapidly around the channel pore (e.g., to 3 μM within ~0.5 ms) at an initial rate that is not appreciably slowed by the presence of buffer. The probability of Ca^{2+} binding to the low-affinity inhibitory binding site during this brief period is very small, so the subunit typically goes to the

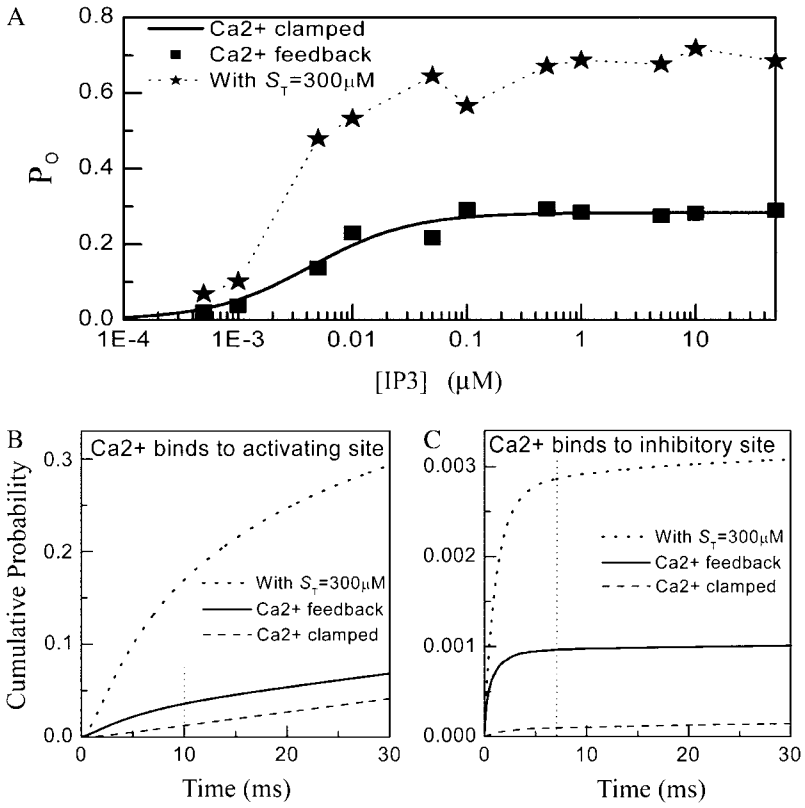

FIGURE 4 Statistical dynamics of the monomeric IP_3R model. (*A*) Channel open probability P_O as a function of $[IP_3]$. The solid line is obtained with $[Ca^{2+}]$ clamped at 0.05 μM; the squares are simulation results with Ca^{2+} feedback in the absence of any Ca^{2+} buffers, and the stars are results with Ca^{2+} feedback in the presence of immobile cytosolic buffer $S_T = 300$ μM. (*B* and *C*) Cumulative probabilities of Ca^{2+} binding to the activating Ca^{2+} site (*B*) and to the inhibitory Ca^{2+} site (*C*) of the monomeric model at increasing times latency after the channel closes. $[IP_3] = 10$ μM. In both panels, the dashed lines are obtained with $[Ca^{2+}]$ clamped at 0.05 μM; the solid curves are calculated with Ca^{2+} feedback in the absence of buffer; and the dotted curves are with Ca^{2+} feedback in the presence of stationary buffer $S_T = 300$ μM.

state (100). However, as shown in Fig. 2, *C* and *D*, increasing concentrations of stationary buffer promote a biphasic decay of local free $[Ca^{2+}]$, and greatly prolong the time for which Ca^{2+} concentrations then remain elevated at a few hundred nM. This Ca^{2+} tail greatly increases the probability that Ca^{2+} will bind to the high-affinity activating site, causing the channel to return to the (110) state and thus reopen (Fig. 4 *B*, *dotted curve*). Although the probability of binding to the inhibitory site is concurrently potentiated, the absolute value remains very small (0.003: Fig. 4 *C*, *dotted curve*), so inhibition is negligible.

These dynamics do not occur for DeYoung-Keizer-type models of the IP_3R (18), which lack the A-state. When such a channel is open (i.e., in 110-state), the local high concentration of Ca^{2+} resulting from flux through the open channel promotes binding to the inhibitory site, forcing the channel into an inhibited state (111) with a long characteristic time (e.g., 0.25 s with $a_2 = 0.04$ $\mu M^{-1}s^{-1}$ and $[Ca^{2+}] = 100$ μM). Once in (111) state, the residual Ca^{2+} tail remaining after the channel closes will have little effect on the channel dynamics. The channel closing in a model without A-state will predominantly involve dissociation of activating Ca^{2+}, i.e., from the open state(110) to the state (100) with a short characteristic time 0.04 s at $b_5 = 24$ s^{-1}, before inhibitory Ca^{2+} has time to bind. Furthermore, the fast transient dynamics between the open state (110) and the state (100) (i.e., the dissociation of activating Ca^{2+}) result again in a bursting behavior.

The complete tetrameric IP_3R model with four subunits

Finally, we consider a complete, multimeric IP_3R model composed from four subunits. A notable functional difference from the single-subunit model results from the assumption that the channel can open when only three subunits are in the active state. Thus, Ca^{2+} binding to the fourth, inactive subunit may now occur as a result of the very high local $[Ca^{2+}]$ established while the channel is open. Similarly, for purposes of comparison, we first discuss the channel dynamics when cytosolic $[Ca^{2+}]$ is fixed at 0.05 μM (Fig. 5, *A* and *B*), and then consider how these dynamics are modified by feedback of Ca^{2+} flowing through the channel in the absence or presence of stationary and mobile Ca^{2+} buffers.

Multimeric channel with fixed cytosolic $[Ca^{2+}]$

For the multimeric IP_3R with $[Ca^{2+}]$ clamped at 0.05 μM, the channel open probability P_O, mean open time τ_O, and mean closed time τ_C are depicted in Fig. 6, *A–C* (*solid squares*), as functions of $[IP_3]$, derived by transition matrix theory (see Appendix C). In comparison to the monomeric model at the equivalent $[IP_3]$, the tetrameric IP_3R model shows a low P_O, since at least three subunits must be in the active state for the channel to open. The channel shows bursting dynamics, with a bimodal distribution of closed times composed from relatively long interburst intervals and shorter closings within

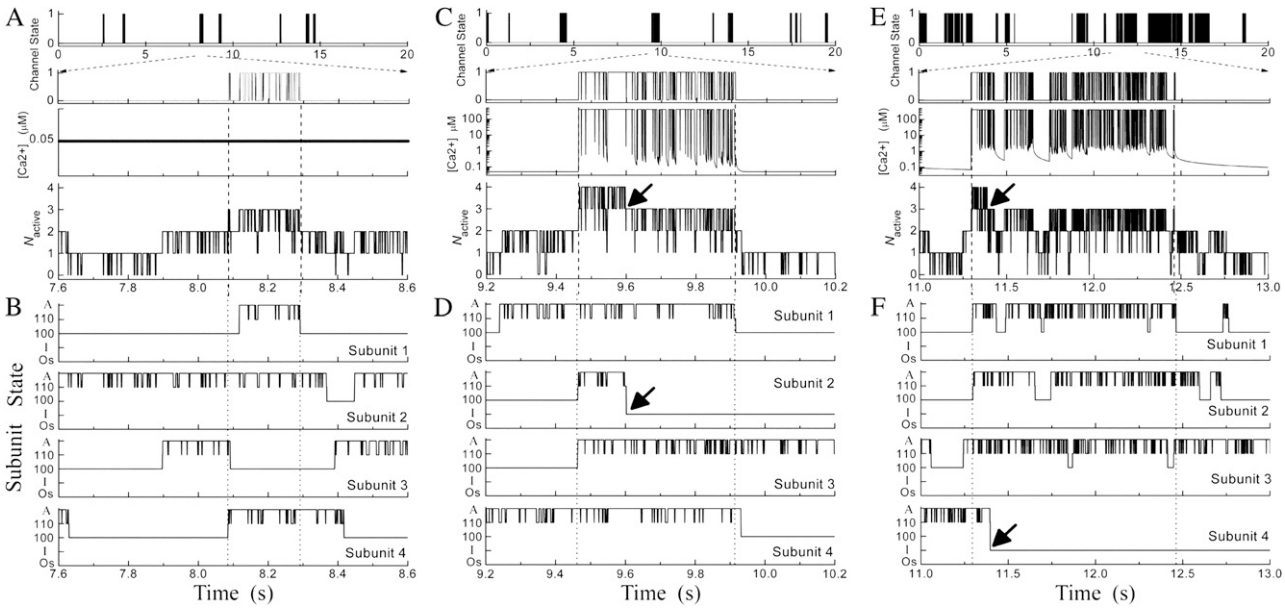

FIGURE 5 Dynamics of the complete, multimeric IP_3R model. (*A*) Representative channel kinetics with $[Ca^{2+}]$ clamped at 0.05 μM. The upper panel illustrates bursting behavior of channel states on a slow timescale; the second panel shows local $[Ca^{2+}]$ at the channel pore and, in gray overlay, channel openings during a single burst at an expanded timescale; the lower panel shows the number of subunits in the active state before, during, and after the burst. (*B*) Panels represent the states of the four subunits corresponding to the burst shown in *A*. (*C* and *D*) Corresponding examples of channel gating, local $[Ca^{2+}]$, and subunit states with Ca^{2+} feedback in the absence of any Ca^{2+} buffer. (*E* and *F*) Corresponding examples of channel gating, local $[Ca^{2+}]$, and subunit states with Ca^{2+} feedback in the presence of stationary buffer $S_T = 300$ μM. In all examples, $[IP_3] = 10$ μM.

bursts. The close time distribution shows a local minimum around 20 ms, and we thus used a criterion of 20 ms to discriminate inter- from intraburst closings. We plot in Fig. 6, *D–F* (*squares*), the mean burst duration (T_{Burst}) and inter- (T_{Inter}) and intraburst (T_{Intra}) intervals as functions of $[IP_3]$. A short $T_{Intra} \sim 2$ ms is obtained, which is determined mainly by $1/a_0 = 1.9$ ms, corresponding to fast transitions between the active state and the closed state (110).

Dynamics of the tetrameric channel with free Ca^{2+} feedback

Next, we consider the dynamics of the multimeric channel with Ca^{2+} as the flux carrier in the absence of any Ca^{2+} buffer. Fig. 5 *C* illustrates channel gating dynamics at $[IP_3] = 10$ μM, together with an expanded view of local $[Ca^{2+}]$ changes and subunit states during a single burst; and Fig. 5 *D* shows the corresponding conformations of each subunit. For this simulation, both the activating and inhibitory binding sites are located at the channel pore, and hence experience maximal changes in $[Ca^{2+}]$ when the channel is open.

During the initial part of the burst, all four subunits are predominantly in the active state, and closings are relatively rare as transition of any single subunit from the active state leaves the channel open. However, after a brief time, one subunit does become Ca^{2+}-inhibited, as marked by arrows (Fig. 5, *C* and *D*). This happens when the channel is open with one subunit in an inactive state, so that the high local $[Ca^{2+}]$ resulting from flux through the open channel results in Ca^{2+} binding to its inhibitory site. Given that the rate of dissociation from the inhibitory site is slow ($\sim 1/b_2 = 1.56$ s), only three subunits then remain available to continue the burst, which ultimately terminates as discussed above for the monomeric channel model. In particular, there is a very low probability that termination results from two or more subunits becoming inhibited, because transition of any of the three remaining active subunits to an inactive state causes the channel to close, resulting in a rapid collapse of the local Ca^{2+} microdomain, leaving little chance for Ca^{2+} to bind to an inactive subunit.

The resulting steady-state channel dynamics and bursting kinetics are plotted as open circles in, respectively, Fig. 6, *A–C* and *D–F*, as functions of $[IP_3]$. Notably, feedback of Ca^{2+} ions flowing through the channel to act on binding sites located at the pore produces only small changes in behavior from the situation when cytosolic $[Ca^{2+}]$ is clamped at the resting level (compare data marked by *squares* and *circles* in Fig. 6).

To help understand this lack of effect, we separately considered the effects of Ca^{2+} feedback on only the activating sites or only the inhibitory sites by clamping $[Ca^{2+}]$ at the other set of sites at 0.05 μM. That is to say, for those sites with clamped $[Ca^{2+}]$, a fixed calcium concentration of $[Ca^{2+}]_{Rest} = 0.05$ μM was used to compute their Ca^{2+}-binding probabilities, whereas for those sites with feedback $[Ca^{2+}]$, a kinetic calcium concentration obtained from the reaction-diffusion equations was used to calculate their

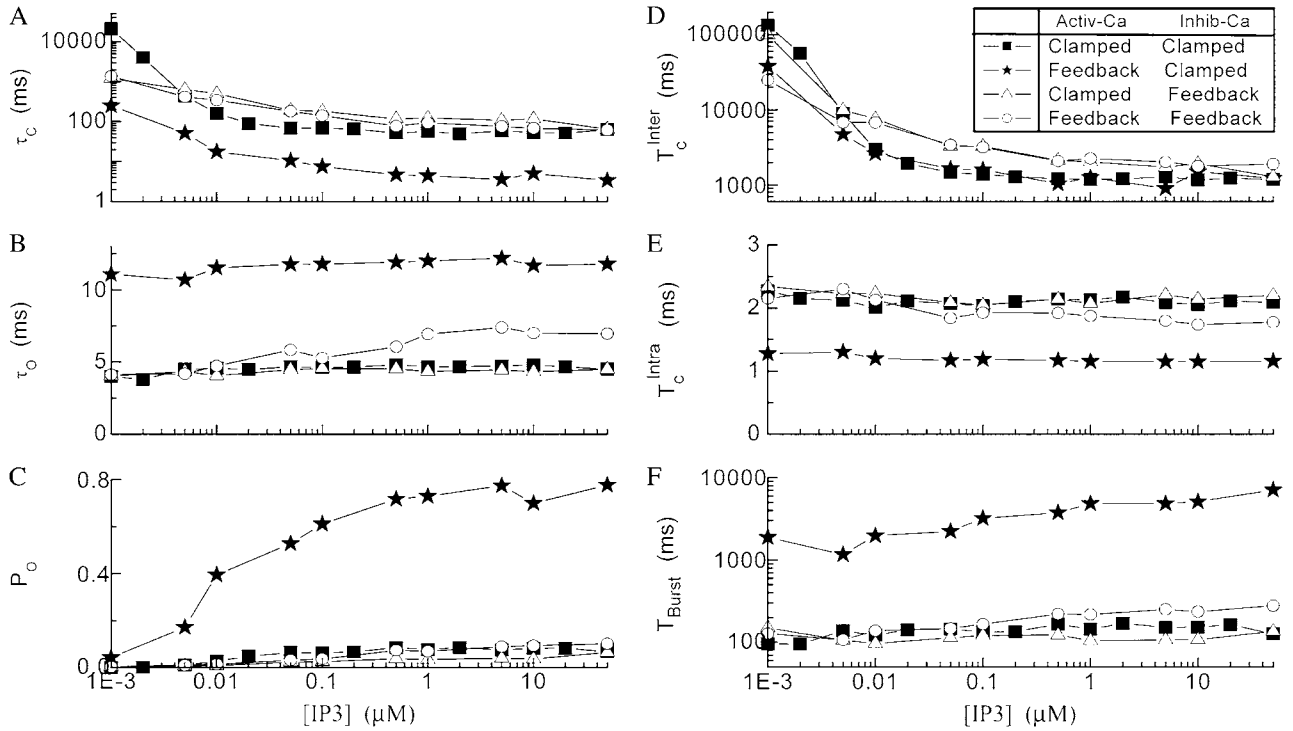

FIGURE 6 Statistical dynamics of the multimeric IP_3R channel in the absence of Ca^{2+} buffer, exploring separately the effects of Ca^{2+} feedback on the activating and inhibitory binding sites located at the channel pore. (*A–C*) Panels show, respectively, the mean channel closed time τ_C, the mean open time τ_O, and the open probability P_O as functions of $[IP_3]$. (*D–F*) Burst dynamics of the channel, derived by setting a criterion of 20 ms to discriminate between short interburst closings and longer intraburst intervals. Panels show, respectively, mean interburst durations, mean intraburst intervals, and mean burst durations as functions of $[IP_3]$. In all panels, the families of curves were obtained by either fixing $[Ca^{2+}]$ at the activating and/or inhibitory binding sites at the resting level, or by allowing Ca^{2+} feedback via flux through the channel. Specifically, squares represent both activating and inhibitory Ca^{2+} binding sites clamped at $[Ca^{2+}] = 0.05\ \mu M$; stars represent inhibitory Ca^{2+} binding sites clamped; triangles represent Ca^{2+} feedback on inhibitory sites with activating sites clamped; and circles represent Ca^{2+} feedback on both activating and inhibitory binding sites.

Ca^{2+}-binding probabilities. Although biologically unrealistic, this is a useful modeling exercise to help dissect out the otherwise intertwined actions of activating and inhibitory Ca^{2+} binding sites; and is equivalent to functionally ''knocking out'' one or other type of site.

The open triangles in Fig. 6 show that feedback exclusively on inhibitory binding sites promotes a slight decrease of P_O (Fig. 6 *C*) and shortening of burst duration (Fig. 6 *F*). This is expected, since one subunit would rapidly become Ca^{2+}-inhibited so that subsequent openings involve three out of three ''activatable'' subunits, rather than three out of four for the case without any Ca^{2+} feedback. More dramatically, however, Ca^{2+} feedback operating exclusively on the activating binding sites results in a roughly 10-fold increase in P_O and lengthening of burst duration (*stars* in Fig. 6). This may be readily understood by first considering the channel in an open state with all four subunits active. Transition of any one subunit to an inactive state and subsequent dissociation of activating Ca^{2+} will very rapidly result in rebinding of Ca^{2+}, since the activating site is exposed to high local $[Ca^{2+}]$ as the remaining three active subunits maintain the channel in the open state. Thus, any subunit that becomes inactive will rapidly reactivate, thereby greatly prolonging bursts of channel openings (Fig. 6 *F*) and correspondingly enhancing P_O (Fig. 6 *C*). This effect is negated, however, when Ca^{2+} feedback is permitted at inhibitory as well as activating binding sites (*circles* in Fig. 6). As soon as a subunit becomes inhibited, it can no longer participate in channel openings, so that transition of any one of the remaining three subunits to an inactive state causes the channel to close. The probability that an inactive subunit will then bind Ca^{2+} from the (100) state and reactivate is small because, as discussed above, this is determined by the lingering tail of $[Ca^{2+}]$ as the microdomain collapses, rather than by the very high local $[Ca^{2+}]$ around an open channel. Due to the fast collapse, the Ca^{2+} tail has little probability of reopening the channel, so that similar dynamics are observed either with $[Ca^{2+}]$ clamped or with Ca^{2+} feedback (*squares* and *circles* in Fig. 6).

Modulation of Ca^{2+} feedback on the tetrameric IP_3R by stationary Ca^{2+} buffer

In this section, we consider the dynamics of the multimeric IP_3R model when the local Ca^{2+} microdomain is modulated by stationary buffer. First, we discuss an example with $[IP_3] = 10\ \mu M$ and $S_T = 300\ \mu M$ (Fig. 5, *E* and *F*). The

presence of stationary buffer results in a marked increase in open probability and a prolongation of burst durations. The distributions of open time duration and close time duration are given in Fig. 7, *A* and *B*, giving an open probability of 0.2 with a mean open time of 5.8 ms and a mean closed time of 25.3 ms. The open and closed times in Fig. 7 are short, presumably reflecting flickering between the A-state and (110) state. Experimental records would probably not resolve these brief transitions, so the apparent blip duration would primarily reflect the longer burst durations.

The actions of stationary buffer likely arise through two principal mechanisms: 1), because the stationary Ca^{2+} buffer causes a slowly decaying tail of free Ca^{2+} after channel closure, there will be an increased likelihood of binding to activating Ca^{2+} sites; and 2), the change in spatial distribution of Ca^{2+} around an open channel may differentially affect binding to the inhibitory sites depending on their distance from the channel pore.

The binding of Ca^{2+} to sites on an inactive subunit of an open channel is expected to be highly sensitive to the location of the sites on the IP_3R in relation to the pore. For example, if a binding site were closely adjacent to the pore, it would sense the peak of the $[Ca^{2+}]$ microdomain ($\sim$400 μM), whereas if it were at the edge of the IP_3R molecule at a distance $R \sim 15$ nm from the pore, the resulting $[Ca^{2+}]$ would be only $\sim$30 μM. On the other hand, the spatial gradient of

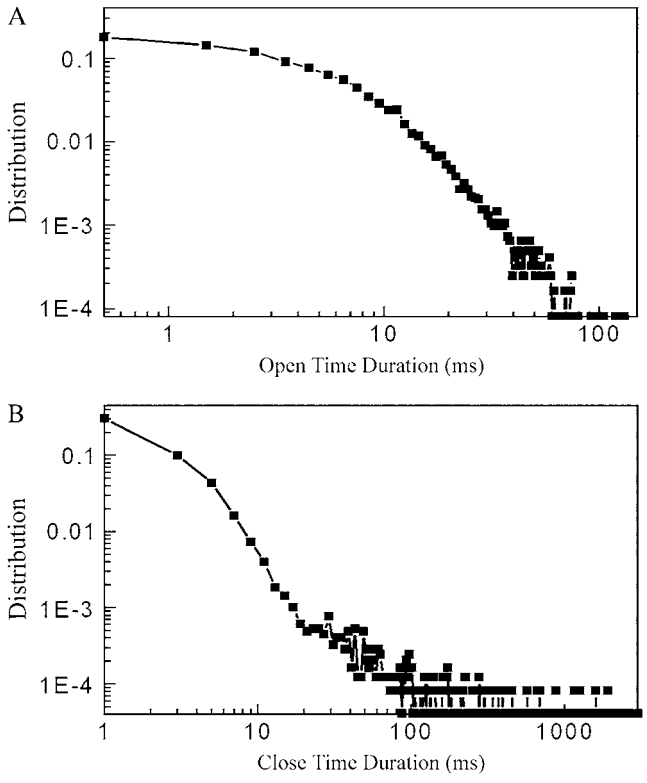

FIGURE 7 Distribution of open (*A*) and closed time durations (*B*) for the multimeric IP_3R model with Ca^{2+} feedback in the presence of immobile buffer. $S_T = 300$ μM and $[IP_3] = 10$ μM.

$[Ca^{2+}]$ equilibrates rapidly after closure of the channel, so that the $[Ca^{2+}]$ sensed by binding sites at the pore or edge of the IP_3R would be closely similar during the tail of residual Ca^{2+} as the microdomain collapses.

We show in Fig. 8 how the channel dynamics are affected by the presence of stationary buffer S_T when the activating and inhibitory binding sites are located at either the pore or the edge of the IP_3R. Fig. 8, *A–C*, plots simulation data as functions of S_T with $[IP_3]$ fixed at 10 μM. One general result is that the mean channel closed time τ_c shortens markedly as S_T is raised from $\sim$100 to 1000 μM (Fig. 8 *A*), resulting in a corresponding increase in P_o (Fig. 8 *C*), since the mean open time T_o shows only slight dependence on buffer concentration (Fig. 8 *B*). The multimeric IP_3R model thus shows qualitatively similar behavior to the simplified monomeric model, in that the slowing of $[Ca^{2+}]$ decay after channel closure promotes binding to activating Ca^{2+} sites and hence increases the probability of reopening. A second major finding is that, at any given S_T, the channel dynamics are highly sensitive to the location of the inhibitory Ca^{2+} binding site, but are almost independent on the location of the activating site. This follows because inhibition is manifest primarily by the steep spatial gradient of Ca^{2+} around an open channel acting on an inactive subunit In contrast, the lack of sensitivity of channel dynamics to the position of the activating Ca^{2+} binding site may be explained by two reasons: 1), during a burst, the reopening of the channel results mainly as subunits transition from the (110) state to the active state, independent of $[Ca^{2+}]$; and 2), initiation of new bursts typically occurs after relatively long interburst intervals when the Ca^{2+} microdomain has collapsed so that little spatial gradient of $[Ca^{2+}]$ remains around the channel.

In Fig. 8, *D–F*, the channel dynamics are plotted as functions of binding and unbinding rates of immobile buffer with S_T fixed at 300 μM. The dissociation constant $K_S = \beta_S/\alpha_S$ is fixed at 2 μM while the on and off binding rates are correspondingly altered. Our simulation results indicate that the channel dynamics are relatively insensitive to the changes in immobile buffer kinetics across a range of binding rates.

Fig. 9, *A–C*, shows the channel dynamics as a function of $[IP_3]$ at the presence of $S_T = 300$ μM. The open probability increases with the increase of $[IP_3]$, reaching saturation at about $[IP_3] = 5$ μM. As a comparison, Fig. 6 *C* (*open circles*) indicates that the open probability becomes saturating at about $[IP_3] = 0.5$ μM in the absence of any Ca^{2+} buffers. Fig. 9 also shows that a larger P_o is obtained for the channel with all Ca^{2+} binding sites at channel edge.

Modulation of Ca^{2+} feedback on the tetrameric IP_3R by mobile Ca^{2+} buffer

We finally discuss how the dynamics of the tetrameric IP_3R model are modulated by introduction of mobile buffer in the presence of stationary buffer for cases where the activating and inhibitory binding sites are located at either the pore or

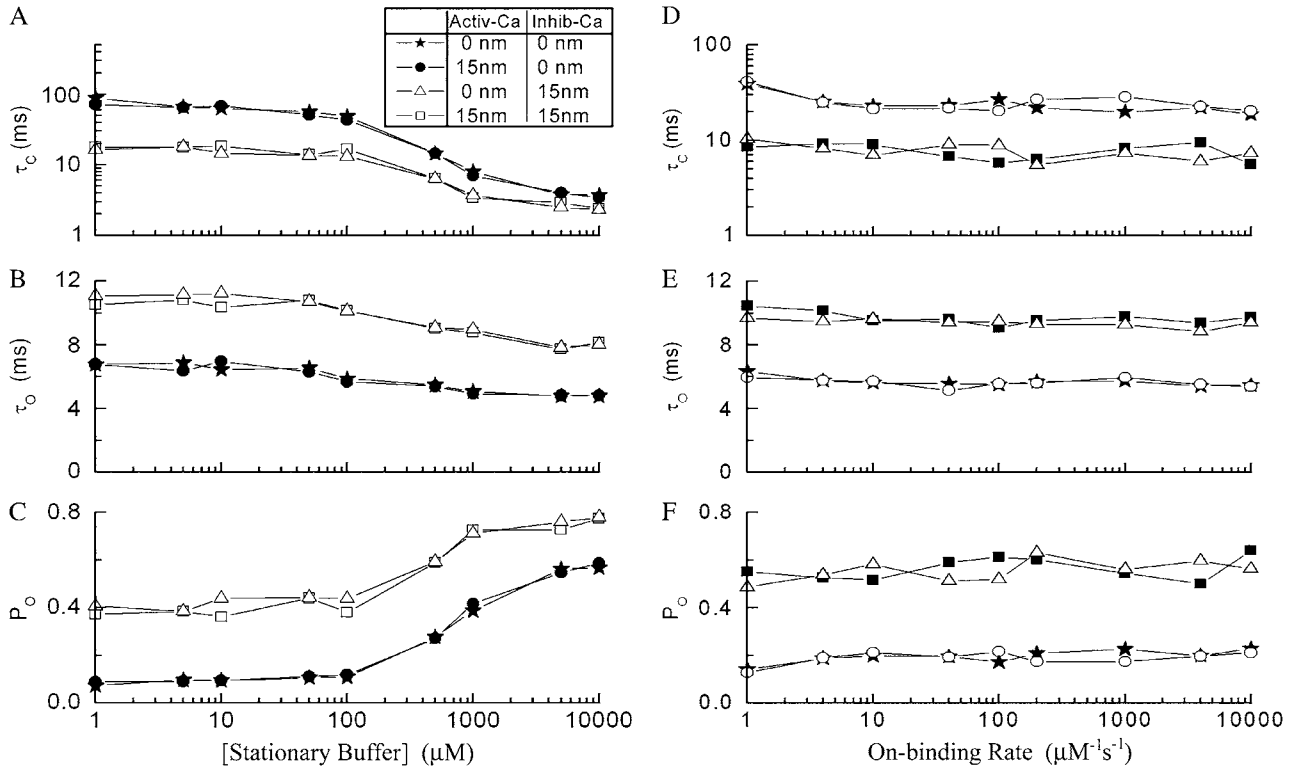

FIGURE 8 Modulation of multimeric IP_3R model dynamics by stationary buffer. (*A–C*) Panels show, respectively, the mean closed time τ_C, mean open time τ_O, and mean open probability P_O as functions of S_T. (*D–F*) Corresponding changes in channel dynamics as functions of Ca^{2+} binding rate to immobile buffer at $S_T = 300\ \mu M$. Here $[IP_3] = 10\ \mu M$. In all cases, Ca^{2+} feedback is operational, with the activating and inhibitory Ca^{2+} binding sites located either at the channel pore ($R = 0$ nm) or at the edge of the IP_3R ($R = 15$ nm). Specifically, stars represent both activating and inhibitory Ca^{2+} binding sites at $R = 0$ nm; circles represent activating binding sites at $R = 15$ nm and inhibitory sites at $R = 0$ nm; squares represent activating sites at $R = 0$ nm and inhibitory sites at $R = 15$ nm; and triangles represent both active and inhibitory Ca^{2+} binding sites at $R = 15$ nm.

the edge of the IP_3R. Fig. 10 shows simulation data as functions of the diffusion coefficient of the mobile buffer D_{MCa} for a fixed concentration $M_T = 300\ \mu M$ (Fig. 10, *A–C*), and as functions of M_T with $D_{MCa} = 15\ \mu m^2/s$ (Fig. 10, *D–F*). In the simulation, $[IP_3] = 10\ \mu M$ and $S_T = 300\ \mu M$.

Fig. 10, *A–C*, shows that the mobile buffers with increasing D_{MCa} causes a progressive increase of mean open and closed times. Because the effect on closed time is greater, the open probability decreases with increasing D_{MCa}. While the channel is open, Ca^{2+} ions that have permeated the channel may bind to either the immobile buffers or the mobile buffers. As a result of its immobility, a much steeper gradient will be established for Ca^{2+}-bound immobile buffers than for Ca^{2+}-bound mobile buffers. Once the channel closes, the lingering tail of $[Ca^{2+}]$ around the channel will result mainly from the release of Ca^{2+} ions from Ca^{2+}-bound immobile buffers. Conversely, mobile buffers will act as a ‘‘‘shuttle’’, tending to distribute free Ca^{2+} more homogeneously in the cytosolic space. Thus, mobile buffers with greater diffusion coefficient will cause the $[Ca^{2+}]$ tail to collapse more rapidly, generating a smaller open probability (Fig. 10 *C*).

Fig. 10, *D–E*, show that increasing mobile buffer concentrations are associated with increasing mean open and closed times. However, in contrast to the effects of stationary buffer, the effects on open and closed times more closely parallel one another, so that the open probability changes only slightly (Fig. 10 *F*).

DISCUSSION

We describe stochastic simulations aimed at understanding how the gating of a single IP_3R channel is modulated by feedback of Ca^{2+} ions that pass through the channel and bind to activating and inhibitory sites on the cytosolic face of the receptor. There are rather few published experimental observations of blips, and in particular no quantitative data are available regarding their kinetics. Thus, our object was not to generate a model that replicated experimental data, but principally to gain an understanding of the mechanisms that underlie their generation.

As with any simulation study (20,21), our conclusions are highly dependent upon the initial premises regarding the structure of the model: in particular that ligand binding to IP_3R subunits is locked when they are in an active configuration, and that opening of the tetrameric receptor/channel may occur when either three or four subunits are active. Nevertheless, these assumptions appear well grounded (34,39), and predictions of how the channel dynamics are

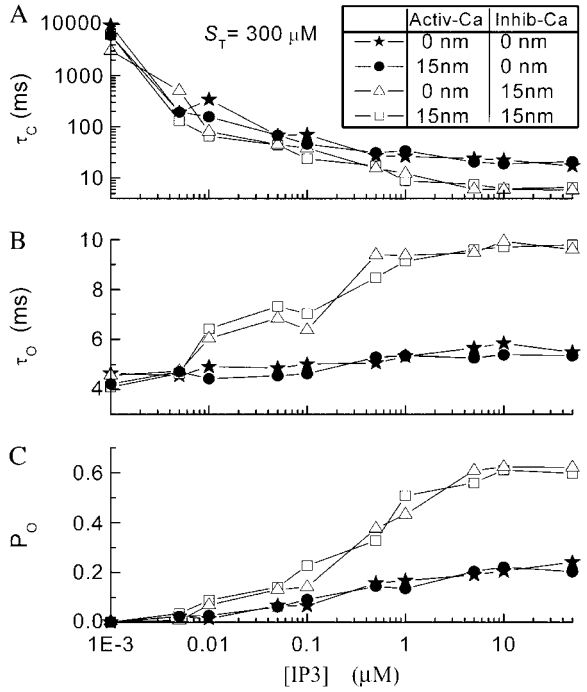

FIGURE 9 Tetrameric IP_3R model dynamics as a function of $[IP_3]$ in the presence of stationary buffer. (*A–C*) Panels show, respectively, the mean closed time τ_C, mean open time τ_O, and mean open probability P_O as functions of $[IP_3]$ at $S_T = 300$ μM. The same notations as in Fig. 8 are used here.

affected by Ca^{2+} feedback may be tested by comparing experimental single-channel data obtained using Ca^{2+} or other ions as the charge carrier.

To facilitate analysis, we first considered a simple IP_3R model composed from a single subunit, and show that freely diffusing Ca^{2+} ions exert negligible effects on channel dynamics despite the very high local Ca^{2+} concentrations attained while the channel is open. The reason lies in our assumption that channel opening involves a conformational change of the subunit to an active state wherein it is locked to binding or dissociation of ligands so that Ca^{2+} binding cannot occur to either the activating or inhibitory sites while the channel is open. This conformational step is analogous to the well-characterized behavior of nicotinic acetylcholine receptors (45), and is consistent with observations of ligand-independent flickering of the IP_3R channel to the closed state (22) and the lack of effect of changes in Ca^{2+} concentration on gating of already open IP_3R channels (46).

Feedback by permeating Ca^{2+} ions is thus restricted to whatever residual Ca^{2+} remains adjacent to the IP_3R after the channel has closed and the subunit has transitioned to an inactive state. If Ca^{2+} ions diffuse freely, the residual microdomain collapses so rapidly that the probability of binding is slight. However, in an intracellular environment, typically only a few percent of cytosolic Ca^{2+} ions are free, with a large fraction being bound reversibly to immobile buffers (47). Addition of immobile buffer to the cytosolic space of our model greatly slows the decline of local $[Ca^{2+}]$ after channel closure, since it acts as a sink to absorb Ca^{2+} while the channel is open, but subsequently as a source after the channel closes. The lingering tail of residual Ca^{2+} thus promotes long bursts of channel activity with reopenings triggered by binding to the high-affinity activating site, whereas the local concentration of $[Ca^{2+}]$ during the tail is too small to cause appreciable binding to the low-affinity inhibitory site. Thus, the overall effect of stationary buffer is to produce a pronounced increase in mean open probability.

The results obtained with the above simplified monomeric model would be generally applicable also to the known tetrameric structure of the IP_3R (4) if channel opening required that all four subunits be in the active conformation. However, we have argued previously (39) that experimental data are best accounted for by assuming that the channel may open if either three or four subunits are active. That property introduces further complexity into the actions of Ca^{2+} feedback on the receptor, because openings that involve only three subunits now expose the activating and inhibitory sites on the remaining (inactive) subunit to binding driven by the extremely high local $[Ca^{2+}]$ around the open pore. The resulting dynamics depend on the balance between binding to the activating and inhibitory sites, which, in turn, depends on their distances from the channel pore.

Distinct from the effect of immobile buffer to increase the channel open probability by building up a lingering $[Ca^{2+}]$ tail, we show that freely mobile buffer acts as a shuttle tending to distribute Ca^{2+} ions more homogeneously and causing the residual $[Ca^{2+}]$ tail to collapse more rapidly after channel closure, thereby decreasing the channel open probability.

Since the molecular architecture of the receptor is poorly characterized with respect to the locations of Ca^{2+} binding sites (4), we explored the extreme cases of locating each site either immediately adjacent to the pore, or at a distance of 15 nm corresponding roughly to the radius of the IP_3R molecule (2). Our results indicate that Ca^{2+} feedback on the multimeric IP_3R model is highly sensitive to the location of the inhibitory Ca^{2+} binding site. Because of its low affinity, Ca^{2+} binding is appreciable only within the peak of the microdomain around an open channel, and is negligible after channel closure. An inhibitory site located near the pore of an inactive subunit thus rapidly binds Ca^{2+} while the channel is open and, coupled with the slow rate for dissociation, ensures that one subunit in the tetramer is predominantly in an inhibited state. On the other hand, location of the inhibitory site at the edge of the IP_3R appreciably reduces the likelihood of inhibitory Ca^{2+} binding, thereby increasing the probability that a subunit that enters the (100) state while the channel is still open will rapidly bind Ca^{2+} at the activating site and return to the active configuration rather than becoming inhibited.

The multimeric IP_3R model thus displays two forms of Ca^{2+} feedback activation: i), feedback by residual Ca^{2+} by

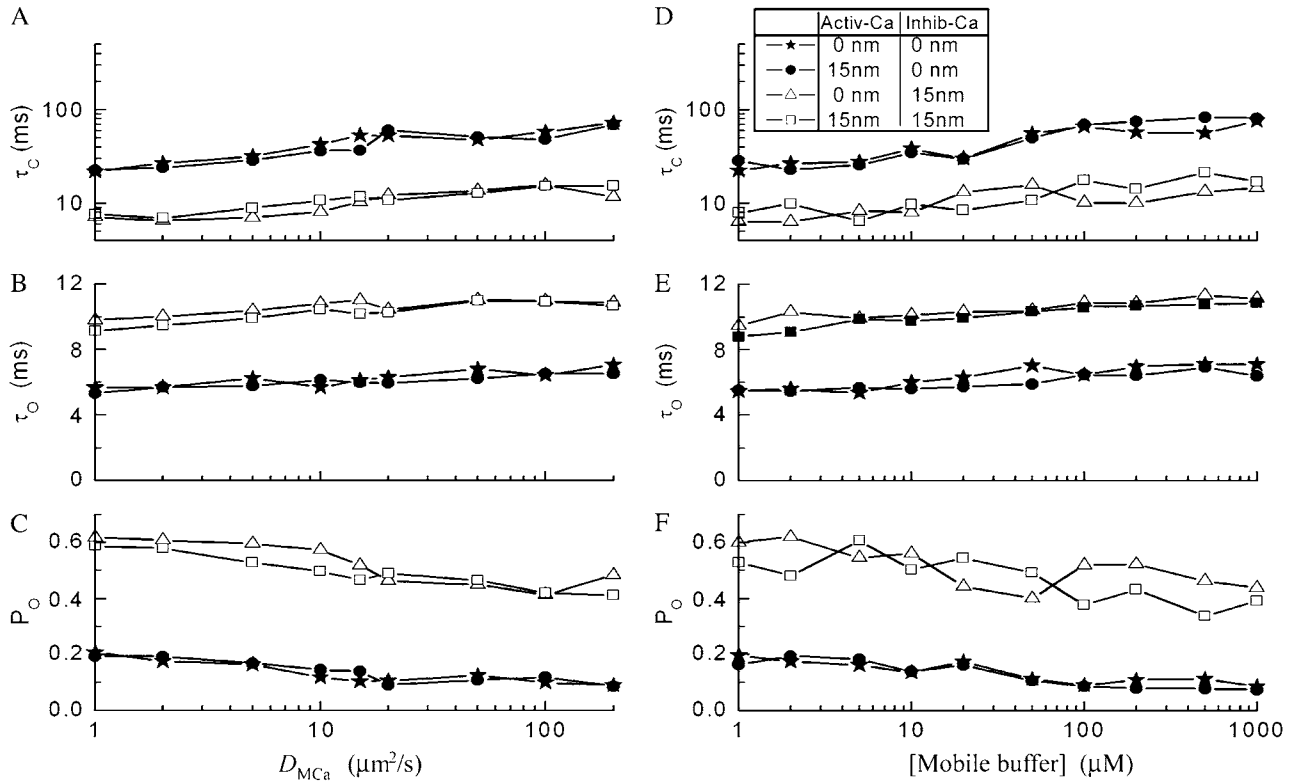

FIGURE 10 Modulation of multimeric IP_3R model dynamics by mobile buffer. (*A–C*) Panels show, respectively, the mean closed time τ_C, mean open time τ_O, and mean open probability P_O as functions of diffusion coefficient of the mobile buffer D_{MCa} for $M_T = 300$ μM. (*D–F*) Corresponding changes in channel dynamics as functions of mobile buffer concentration M_T for $D_{MCa} = 15$ $\mu m^2/s$. $[IP_3] = 10$ μM. The same notations as in Fig. 8 are used here.

binding to activating sites on inactive subunits after the channel has closed, which is significant only in the presence of stationary buffers; and ii), feedback on the activating site of a single inactive subunit of an open channel by Ca^{2+} ions directly flowing through that channel. In both of these cases, the location of the activating Ca^{2+} site—in contrast to the inhibitory site—is inconsequential. This follows because the affinity of the activating site is sufficiently high so that binding is effectively saturated over distances of many tens of nm from the pore while a channel is open; whereas after closure the spatial gradient of the residual microdomain rapidly flattens, so there is little difference in $[Ca^{2+}]$ across the dimensions of a single IP_3R molecule.

Swillens et al. (33) previously considered the behavior of a monomeric IP_3R model within a cytosol-like environment, and proposed that the relatively long durations of single-IP_3R blip events observed by intracellular imaging (6) could be reconciled with the much shorter open channel times recorded in bilayer and patch-clamp systems (13,48) because the high concentration of Ca^{2+} at the channel mouth just after closure promotes rebinding that leads to prolonged bursts of activity. Our simulations show that the burst dynamics can still be observed even for the IP_3R model in which a conformational change has been considered before the IP_3R opens. Furthermore, we demonstrate the crucial importance of stationary intracellular buffers in modulating the calcium feedback, and reveal further complexities in channel function when considering a full, tetrameric IP_3R structure.

The cellular environment contains, of course, not just a single IP_3R, but myriad receptors, packed in a densely clustered organization (4). Ca^{2+}-mediated interactions between these receptors underlie the complex patterns of local Ca^{2+} puffs and global cellular waves signals, and will differ markedly from self-feedback on an isolated IP_3R in that neighboring closed channels will be sensitive to Ca^{2+} flux through an open channel that is insensitive to its own Ca^{2+}. Such complex spatiotemporal interactions are the focus of our current efforts using finite element algorithms (34) to extend our IP_3R model to the multiscale environments of channel clusters, aimed at explaining phenomena including the recruitment (25) and termination of IP_3R (49) during Ca^{2+} puffs and the lateral inhibition of IP_3R (46).

APPENDIX A: THE DEPENDENCE OF P_O ON $[IP_3]$ FOR THE MONOMERIC IP_3R MODEL

The probability of the monomeric IP_3R existing in state (*ijk*) or (A) is denoted by P_{ijk} or P_A with $P_A + \sum P_{ijk} = 1$. By the mass action kinetics, the equations describing the subunit dynamics are written (39):

$$\frac{dP}{dt} = PQ, \tag{A1}$$

where Q is the generator matrix of transition rates and P is the vector of probability of subunits. The open probability for an IP_3R is then given by:

$$P_O = P_A. \tag{A2}$$

Mathematically, the equilibrium state is defined by $dP/dt = 0$. The equilibrium vector w satisfies $wQ = 0$ according to the transition matrix theory (50). Detailed balance is imposed so we can solve for w by inspection (51). This is done by calculating all probabilities in terms of their probability relative to state (000). These unnormalized probabilities are denoted q_{ijk} with $q_{000} = 1$. Then

$$w_{ijk} = \frac{q_{ijk}}{Z}, \tag{A3}$$

where each component (q_{ijk}/Z) gives the equilibrium probability for state (ijk). Z is the normalization factor defined by $Z = q_A + \sum q_{ijk}$. The equilibrium probability (q_{ijk}) of state (ijk) relative to that of state (000) is just the product of forward to backward rates along any path connecting (000) to (ijk). Thus we can write

$$q_A = \frac{[IP_3] \times [Ca^{2+}]}{K_1 K_5} \times \frac{a_0}{b_0}. \tag{A4}$$

Thus the open probability is expressed as

$$P_O = w_A = \frac{[IP_3] \times [Ca^{2+}]}{K_1 K_5} \times \frac{a_0}{b_0} \times \frac{1}{Z} \tag{A5}$$

with

$$\begin{aligned} Z = &\left(1 + \frac{[Ca^{2+}]}{K_4}\right)\left(1 + \frac{[Ca^{2+}]}{K_5}\right) \\ &+ \frac{[IP_3]}{K_1}\left(1 + \frac{[Ca^{2+}]}{K_2}\right)\left(1 + \frac{[Ca^{2+}]}{K_5}\right) \\ &+ \frac{[IP_3] \times [Ca^{2+}]}{K_1 K_5} \times \frac{a_0}{b_0} \end{aligned} \tag{A6}$$

resulting in a dependence of P_O on $[IP_3]$ as shown by the solid curve in Fig. 4 *A*.

APPENDIX B: THE CUMULATIVE PROBABILITY FOR THE MONOMERIC IP_3R MODEL

To calculate the cumulative probabilities of Ca^{2+} binding to the activating sites or inhibitory sites (Fig. 4, *B* and *C*), we compute the time duration of the IP_3R channel from the moment of channel closing (i.e., from state A to state 110) to the moment of the first event that a Ca^{2+} ion binds to the activating binding site (i.e., from state 100 to state 110, or from state 000 to state 010) or binds to the inhibitory binding site (i.e., jumping to state 111, 101, 011, or 001). In the simulation 2×10^6 events are simulated and the statistical distributions of time duration for Ca^{2+} activation and inhibition can be calculated. The cumulative probabilities of activation and inhibition are then obtained with an integral process for the time duration distributions from duration 0 to a certain time interval.

In the case of clamped $[Ca^{2+}]$, we have fixed $[Ca^{2+}]$ at 0.05 μM. In the case of considering Ca^{2+} feedback with or without buffer, we simply assume that a steady state of Ca^{2+} distribution has always been achieved before the channel closes. Thus, once the channel closed, the Ca^{2+} concentration collapses with time along a fixed path in the absence or in the presence of buffer, respectively

APPENDIX C: THE DEPENDENCE OF P_O ON $[IP_3]$ FOR THE TETRAMERIC IP_3R MODEL

For the tetrameric IP_3R model, the channel opens when three out of four subunits are in the active state, so

$$P_O = w_A^4 + 4w_A^3(1 - w_A). \tag{A7}$$

Because channel states (A, A, A, not-A) are the only open states that connect to closed channel states by any one of three A-states changing to the closed state 110 with rate b_0, we can directly write the equilibrium probability flux between open and closed states as follows:

$$J = 3b_0 p_3. \tag{A8}$$

The mean open and closed times are given by

$$\begin{aligned} \tau_O &= \frac{P_O}{J} = \frac{1}{3b_0} \times \frac{P_O}{4w_A^3(1 - w_A)} \\ \tau_C &= \frac{1 - P_O}{J} = \frac{1}{3b_0} \times \frac{1 - P_O}{4w_A^3(1 - w_A)}. \end{aligned} \tag{A9}$$

The mean τ_O (~4.5 ms given in Fig. 6 *B* with *solid squares*) remains almost constant because at $[Ca^{2+}] = 0.05$ μM, w^4 is given by $([Ca^{2+}])^4$, and is thus very small in comparison to $1/(3b_0) = 4.2$ ms.

This work was supported by National Institutes of Health grants GM65830 and GM48071. J.S. also acknowledges support from the National Science Foundation of China under grant No. 10775114.

REFERENCES

1. Bezprozvanny, I. 2005. The inositol 1,4,5-trisphosphate receptors. *Cell Calcium.* 38:261–272.
2. Taylor, C. W., P. C. da Fonseca, and E. P. Morris. 2004. IP_3 receptors: the search for structure. *Trends Biochem. Sci.* 29:210–219.
3. Berridge, M. J. 1993. Inositol trisphosphate and calcium signalling. *Nature.* 361:315–325.
4. Foskett, J. K., C. White, K. H. Cheung, and D. O. Mak. 2007. Inositol trisphosphate receptor Ca^{2+} release channels. *Physiol. Rev.* 87:593–658.
5. Bootman, M., E. Niggli, M. Berridge, and P. Lipp. 1997. Imaging the hierarchical Ca^{2+} signalling system in HeLa cells. *J. Physiol.* 499: 307–314.
6. Parker, I., J. Choi, and Y. Yao. 1996. Elementary events of $InsP_3$-induced Ca^{2+} liberation in *Xenopus* oocytes: hot spots, puffs and blips. *Cell Calcium.* 20:105–121.
7. Parker, I., and Y. Yao. 1996. Ca^{2+} transients associated with openings of inositol trisphosphate-gated channels in *Xenopus* oocytes. *J. Physiol.* 491:663–668.
8. Parker, I. and Y. Yao. 1991. Regenerative release of calcium from functionally discrete subcellular stores by inositol trisphosphate. *Proc. R. Soc. Lon. B.* 246:269–74.
9. Sun, X. P., N. Callamaras, J. S. Marchant, and I. Parker. 1998. A continuum of $InsP_3$-mediated elementary Ca^{2+} signalling events in *Xenopus* oocytes. *J. Physiol.* 509:67–80.
10. Callamaras, N., J. S. Marchant, X. P. Sun, and I. Parker. 1998. Activation and co-ordination of $InsP_3$-mediated elementary Ca^{2+} events during global Ca^{2+} signals in *Xenopus* oocytes. *J. Physiol.* 509:81–91.
11. Bootman, M. D., M. J. Berridge, and P. Lipp. 1997. Cooking with calcium: the recipes for composing global signals from elementary events. *Cell.* 91:367–373.
12. Dellis, O., S. G. Dedos, S. C. Tovey, R. Taufiq Ur, S. J. Dubel, and C. W. Taylor. 2006. Ca^{2+} entry through plasma membrane IP_3 receptors. *Science.* 313:229–233.

13. Bezprozvanny, I., J. Watras, and B. E. Ehrlich. 1991. Bell-shaped calcium-response curves of Ins(1,4,5)P_3- and calcium-gated channels from endoplasmic reticulum of cerebellum. *Nature*. 351:751–754.

14. Mak, D. O., S. McBride, and J. K. Foskett. 1998. Inositol 1,4,5-trisphosphate activation of inositol trisphosphate receptor Ca^{2+} channel by ligand tuning of Ca^{2+} inhibition. *Proc. Natl. Acad. Sci. USA*. 95: 15821–15825.

15. Dargan, S. L., and I. Parker. 2003. Buffer kinetics shape the spatiotemporal patterns of IP_3-evoked Ca^{2+} signals. *J. Physiol*. 553:775–788.

16. Dargan, S. L., B. Schwaller, and I. Parker. 2004. Spatiotemporal patterning of IP_3-mediated Ca^{2+} signals in *Xenopus* oocytes by Ca^{2+}-binding proteins. *J. Physiol*. 556:447–461.

17. Xu, T., M. Naraghi, H. G. Kang, and E. Neher. 1997. Kinetic studies of Ca^{2+} binding and Ca^{2+} clearance in the cytosol of adrenal chromaffin cells. *Biophys. J*. 73:532–545.

18. De Young, G. W., and J. Keizer. 1992. A single-pool inositol 1,4,5-trisphosphate-receptor-based model for agonist-stimulated oscillations in Ca^{2+} concentration. *Proc. Natl. Acad. Sci. USA*. 89:9895–9899.

19. Sneyd, J., and J. F. Dufour. 2002. A dynamic model of the type-2 inositol trisphosphate receptor. *Proc. Natl. Acad. Sci. USA*. 99:2398–2403.

20. Sneyd, J., and M. Falcke. 2005. Models of the inositol trisphosphate receptor. *Prog. Biophys. Mol. Biol*. 89:207–245.

21. Sneyd, J., M. Falcke, J. F. Dufour, and C. Fox. 2004. Comparison of three models of the inositol trisphosphate receptor. *Prog. Biophys. Mol. Biol*. 85:121–140.

22. Mak, D. O., S. M. McBride, and J. K. Foskett. 2003. Spontaneous channel activity of the inositol 1,4,5-trisphosphate ($InsP_3$) receptor ($InsP_3R$). Application of allosteric modeling to calcium and $InsP_3$ regulation of $InsP_3R$ single-channel gating. *J. Gen. Physiol*. 122: 583–603.

23. Fraiman, D., and S. P. Dawson. 2004. A model of the IP_3 receptor with a luminal calcium binding site: stochastic simulations and analysis. *Cell Calcium*. 35:403–413.

24. Shuai, J. W., and P. Jung. 2002. Stochastic properties of Ca^{2+} release of inositol 1,4,5-trisphosphate receptor clusters. *Biophys. J*. 83:87–97.

25. Swillens, S., G. Dupont, L. Combettes, and P. Champeil. 1999. From calcium blips to calcium puffs: theoretical analysis of the requirements for interchannel communication. *Proc. Natl. Acad. Sci. USA*. 96:13750–13755.

26. Thul, R., and M. Falcke. 2004. Release currents of IP_3 receptor channel clusters and concentration profiles. *Biophys. J*. 86:2660–2673.

27. Ullah, G., and P. Jung. 2006. Modeling the statistics of elementary calcium release events. *Biophys. J*. 90:3485–3495.

28. Falcke, M. 2003. On the role of stochastic channel behavior in intracellular Ca^{2+} dynamics. *Biophys. J*. 84:42–56.

29. Falcke, M., M. Or-Guil, and M. Bar. 2000. Dispersion gap and localized spiral waves in a model for intracellular Ca^{2+} dynamics. *Phys. Rev. Lett*. 84:4753–4756.

30. Means, S., A. J. Smith, J. Shepherd, J. Shadid, J. Fowler, R. J. H. Wojcikiewicz, T. Mazel, G. D. Smith, and B. S. Wilson. 2006. Reaction diffusion modeling of calcium dynamics with realistic ER geometry. *Biophys. J*. 91:537–557.

31. Shuai, J. W., and P. Jung. 2003. Optimal ion channel clustering for intracellular calcium signaling. *Proc. Natl. Acad. Sci. USA*. 100:506–510.

32. Dawson, S. P., J. Keizer, and J. E. Pearson. 1999. Fire-diffuse-fire model of dynamics of intracellular calcium waves. *Proc. Natl. Acad. Sci. USA*. 96:6060–6063.

33. Swillens, S., P. Champeil, L. Combettes, and G. Dupont. 1998. Stochastic simulation of a single inositol 1,4,5-trisphosphate-sensitive Ca^{2+} channel reveals repetitive openings during 'blip-like' Ca^{2+} transients. *Cell Calcium*. 23:291–302.

34. Rudiger, S., J. W. Shuai, W. Huisinga, C. Nagaiah, G. Warnecke, I. Parker, and M. Falckey. 2007. Hybrid stochastic and deterministic simulations of calcium blips. *Biophys. J*. 93:1847–1857.

35. Wagner, J., and J. Keizer. 1994. Effects of repid buffers on Ca^{2+} diffusion and Ca^{2+} oscillations. *Biophys J*. 67:447–456.

36. Smith, G. D. 1996. Analytical steady-state solution to the rapid buffering approximation near an open Ca^{2+} channel. *Biophys. J*. 71:3064–3072.

37. Smith, G. D., J. Wagner, and J. Keizer. 1996. Validity of the rapid buffering approximation near a point source of calcium ions. *Biophys. J*. 70:2527–2539.

38. Falcke, M. 2003. Buffers and oscillations in intracellular Ca^{2+} dynamics. *Biophys. J*. 84:28–41.

39. Shuai, J., J. E. Pearson, J. K. Foskett, D. O. Mak, and I. Parker. 2007. A kinetic model of single and clustered IP_3 receptors in the absence of Ca^{2+} feedback. *Biophys. J*. 93:1151–1162.

40. Rose, H. J., S. Dargan, J. W. Shuai, and I. Parker. 2006. 'Trigger' events precede calcium puffs in *Xenopus* oocytes. *Biophys. J*. 91:4024–4032.

41. Shuai, J., H. J. Rose, and I. Parker. 2006. The number and spatial distribution of IP_3 receptors underlying calcium puffs in *Xenopus* oocytes. *Biophys. J*. 91:4033–4044.

42. Shuai, J., and I. Parker. 2005. Optical single-channel recording by imaging Ca^{2+} flux through individual ion channels: theoretical considerations and limits to resolution. *Cell Calcium*. 37:283–299.

43. Callamaras, N., and I. Parker. 2000. Phasic characteristic of elementary Ca^{2+} release sites underlies quantal responses to IP(3). *EMBO J*. 19: 3608–3617.

44. Mak, D. O. D., J. E. Pearson, K. P. C. Loong, S. Datta, M. Fernandez-Mongil, and J. K. Foskett. 2007. Rapid ligand-regulated gating kinetics of single inositol 1,4,5-trisphosphate receptor Ca^{2+} release channels. *EMBO Rep*. 8:1044–1051.

45. Hille, B. 2001. Ion Channels of Excitable Membranes, 3rd ed. Sinauer Associates, Sunderland, MA.

46. Adkins, C. E., and C. W. Taylor. 1999. Lateral inhibition of inositol 1,4,5-trisphosphate receptors by cytosolic Ca^{2+}. *Curr. Biol*. 9:1115–1118.

47. Naraghi, M., T. H. Muller, and E. Neher. 1998. Two-dimensional determination of the cellular Ca^{2+} binding in bovine chromaffin cells. *Biophys. J*. 75:1635–1647.

48. Bezprozvanny, I., and B. E. Ehrlich. 1994. Inositol (1,4,5)-trisphosphate ($InsP_3$)-gated Ca channels from cerebellum: conduction properties for divalent cations and regulation by intraluminal calcium. *J. Gen. Physiol*. 104:821–856.

49. Huertas, M. A., and G. D. Smith. 2007. The dynamics of luminal depletion and the stochastic gating of Ca^{2+}-activated Ca^{2+} channels and release sites. *J. Theor. Biol*. 246:332–354.

50. Bruno, W. J., J. Yang, and J. E. Pearson. 2005. Using independent open-to-closed transitions to simplify aggregated Markov models of ion channel gating kinetics. *Proc. Natl. Acad. Sci. USA*. 102:6326–6331.

51. Yang, J., W. J. Bruno, W. S. Hlavacek, and J. E. Pearson. 2006. On imposing detailed balance in complex reaction mechanisms. *Biophys. J*. 91:1136–1141.